

## Surface evolution of crystalline SrTiO<sub>3</sub>, LaAlO<sub>3</sub> and Y<sub>3</sub>Al<sub>5</sub>O<sub>12</sub> targets during pulsed laser ablation

Florian Jung, Ralph Delmdahl, Andreas Heymann, Max Fischer, Helmut Karl

### Angaben zur Veröffentlichung / Publication details:

Jung, Florian, Ralph Delmdahl, Andreas Heymann, Max Fischer, and Helmut Karl. 2022. "Surface evolution of crystalline SrTiO<sub>3</sub>, LaAlO<sub>3</sub> and Y<sub>3</sub>Al<sub>5</sub>O<sub>12</sub> targets during pulsed laser ablation." *Applied Physics A* 128 (9): 750. <https://doi.org/10.1007/s00339-022-05805-5>.



# Surface evolution of crystalline SrTiO<sub>3</sub>, LaAlO<sub>3</sub> and Y<sub>3</sub>Al<sub>5</sub>O<sub>12</sub> targets during pulsed laser ablation

Florian Jung<sup>1</sup> · Ralph Delmdahl<sup>2</sup> · Andreas Heymann<sup>2</sup> · Max Fischer<sup>2</sup> · Helmut Karl<sup>1</sup>

Received: 30 March 2022 / Accepted: 6 June 2022 / Published online: 5 August 2022  
© The Author(s) 2022

## Abstract

Pulsed laser ablation and deposition find applications in various technological and scientific fields, where precise control of the laser target interaction is crucial for achieving reproducible results. In this work, we investigated pulsed laser ablation of single crystalline (001), (011) and (111) oriented SrTiO<sub>3</sub> (STO), (102) LaAlO<sub>3</sub> (LAO) and (001) Y<sub>3</sub>Al<sub>5</sub>O<sub>12</sub> (YAG) targets. The morphology, oxygen loss, and crack formation on the target surfaces after irradiation with a series of KrF excimer laser pulses will be discussed. The target surface morphology was imaged by atomic force, scanning electron microscopy and confocal laser scanning microscopy. Electron backscatter diffraction analysis and energy-dispersive X-ray spectroscopy were used to analyze the crystallographic changes of the surface and the elemental composition. The target material STO shows a significant crack formation and layer separation increasing with surface crystal orientation from (001) through (011) to (111) and laser pulse fluence. In contrast, the laser-ablated surfaces of LAO show only thin hairline cracks and YAG stays free of cracks in the whole laser fluence range investigated but presents large chipped areas.

**Keywords** Pulsed UV laser ablation · Target laser interaction · Complex oxides · Single crystalline targets

## 1 Introduction

Pulsed laser deposition (PLD) based on pulsed laser ablation or sputtering is a highly versatile and flexible thin-film deposition technique for complex multi-component metallic and dielectric materials. Short, high-intensity laser pulses with a duration of 20 ns to 30 ns and energy of several 100 mJ per pulse in the case of excimer lasers and ≈100 fs with an energy of several mJ in case of mode-locked Ti-sapphire

laser systems are consecutively absorbed in a small surface volume at the target surface, resulting in the removal of the target material due to the high energy density deposited [1–3].

In particular, PLD proved ideal for stoichiometric deposition and epitaxial growth of complex oxides in heterostructures [4]. It is an extraordinarily reliable technique and allows processing in different reactive atmospheres up to pressures of more than 100 Pa. The ablated material is emitted into a relatively well confined solid angle partially visible by the emitted light of the generated plasma, called plasma plume. Scanning can achieve homogeneous thin films on tape and large substrates with minimal material loss.

In the case of fs-laser ablation, the extremely high power per pulse > 10<sup>11</sup> W is the dominant driver for nonlinear absorption effects, whereas, in the case of ns-laser ablation, short wavelengths in the UV regime in connection with high power pulses of > 10<sup>7</sup> W are needed to initiate the ablation process. Ablation with fs-laser pulses decouples light absorption from thermalization and subsequent material ablation. In contrast, in the case of ns-laser pulses, the photons interact during the whole duration of the laser pulse with the target material, generating free charge carriers and finally with the plasma directly above the target surface.

✉ Helmut Karl  
Helmut.Karl@physik.uni-augsburg.de

Florian Jung  
Florian.Jung@physik.uni-augsburg.de

Ralph Delmdahl  
Ralph.Delmdahl@coherent.com

Andreas Heymann  
Andreas.Heymann@coherent.com

Max Fischer  
Max.Fischer@coherent.com

<sup>1</sup> Institute of Physics, University of Augsburg, Universitätsstr. 1, Augsburg 86159, Germany

<sup>2</sup> Coherent LaserSystems GmbH & Co. KG, Hans-Böckler-Str. 12, Göttingen 37079, Germany

The absorption in dielectrics begins with the generation of free charge carriers, which results in a significant change in the refractive index by increasing the imaginary part. Multiphoton absorption is needed for photon energies below the bandgap, whereas interband transitions can occur directly for above bandgap energy photons. These initial processes are very fast, followed by further heating of the generated free charge carriers by the laser pulse. Finally, the deposited energy is transferred into the phonon system and leads to the desired ablation of the target material.

Among others, excimer lasers are working with excited dimers of XeCl, KrF, and ArF emitting laser light pulses with wavelengths of 308, 248, and 193 nm, which correspond to photon energies of 4, 5 and 6.5 eV, respectively. Excimer lasers typically emit multimode pulsed beams with cross-sections depending on the design of the laser cavity and particularly on the geometry of the discharge electrodes. Directly focusing by either a cylindrical or spherical lens to a line or spot is often performed, giving rise to inhomogeneous fluences and thus laterally varying ablation conditions, ranging continuously from optimal ablation to sub-threshold laser fluences at the target surface.

In this work, we concentrate on laser ablation of surfaces of oriented single crystals SrTiO<sub>3</sub> (STO), LaAlO<sub>3</sub> (LAO), and Y<sub>3</sub>Al<sub>5</sub>O<sub>12</sub> (YAG) by a pulsed laser beam of a KrF excimer laser with a homogenous areal energy density. Single crystals exhibit accurate cation stoichiometry, are less prone to particle debris formation—as is often the case with sintered polycrystalline targets—and provide a defined initial surface finish. Moreover, they are of great importance for

the growth of functional LAO/STO heterostructures and, in the case of YAG together with Y<sub>3</sub>Fe<sub>5</sub>O<sub>12</sub>, crucial for the development of devices in the field of quantum information processing [5–7].

## 2 Experimental

A KrF excimer laser COMPex 205 F from Coherent was used in this work. The pulse energy was set to 550 mJ with a laser pulse duration of  $\approx 26$  ns throughout the investigations presented. The cross-sectional dimensions of the multimode laser pulses at the exit of the laser cavity is  $\approx 10 \times 24$  mm<sup>2</sup> measured at FWHM. The scheme of the laser beam path is depicted in Fig. 1b. After the laser beam has passed through a continuously adjustable dielectric attenuator, it is focused (focus lens) onto a rectangular aperture with an open width of  $3 \times 9$  mm<sup>2</sup>. The aperture is positioned so that the rim of the flat-top laser beams cross-section is blanked out. The aperture opening is then imaged onto the PLD target surface by the imaging lens at a reduction ratio of 5 to 1. The fluence was controlled solely by a dielectric attenuator and not by the laser system settings to avoid changes in the laser pulse duration, shape and homogeneity across the laser pulse cross-section.

The laser pulse energies were measured by an energy monitor directly after the entrance window of the deposition chamber. The actual laser pulse fluence on the target surface was calculated according to the area of the produced ablation

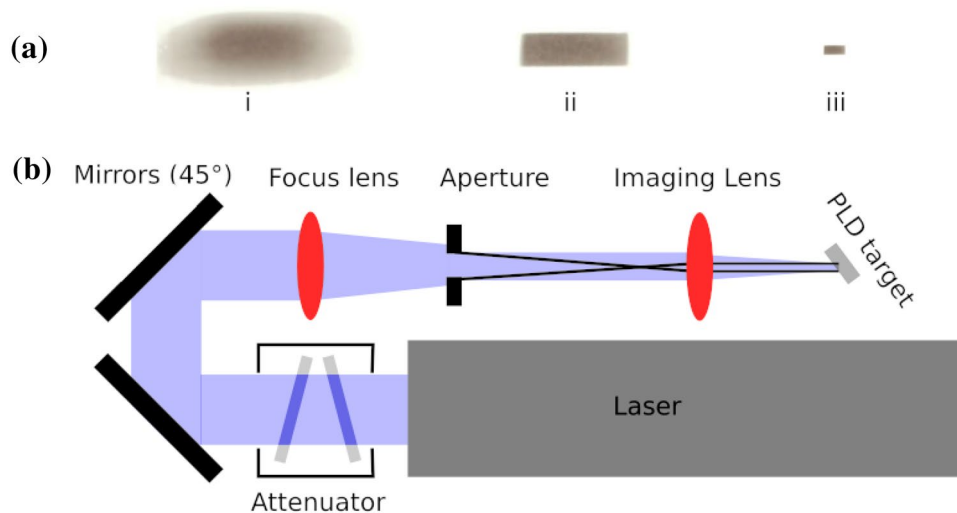


**Fig. 1** **a** Attenuated laser pulse fluence profiles registered with thermal paper before the aperture (i), after the aperture (ii), and at the PLD target (iii)(the proportions are correct the scaling is not). **b** Scheme of the laser beam path with adjustable dielectric attenuator, followed by dielectric mirrors (not shown: additional mirrors,

PLD chamber, and beam entrance window), a focus lens, which reduces the laser beam cross-section at the aperture. The aperture is positioned so that the area of homogeneous laser fluence meets the aperture opening. An image of the aperture is then projected onto the PLD target at a ratio of 5 to 1

**Table 1** Thermophysical properties of the PLD targets

| Target material | Thermal conductivity [W K <sup>-1</sup> m] | Expansion coefficient [K]                         | Melting temperature [°C] | Mohs hardness |
|-----------------|--------------------------------------------|---------------------------------------------------|--------------------------|---------------|
| STO             | 12 [8]                                     | $3 \times 10^{-5}$ [9] $3.87 \times 10^{-5}$ [10] | 2080 [11]                | 6 [12]        |
| LAO             | 10 [13]                                    | $5.5 \times 10^{-6}$ to $6.5 \times 10^{-6}$ [14] | 2134 [15]                | 6.5 [16]      |
| YAG             | 12 [17–19],                                | $8 \times 10^{-6}$ [19]                           | 1940 [20]                | 8.5 [21]      |

crater. The fluences at the target surface were chosen to be 1 to 6 J cm<sup>-2</sup> in 1 J cm<sup>-2</sup> steps.

A polycarbonate target was used for bench-marking the energy density distribution and image quality. Each ablation crater was created by applying 30 laser pulses of constant laser fluence to the initially mirror-polished target surface. The laser pulse repetition rate was 1 Hz and the oxygen pressure was 0.1 Pa. The resulting ablation crater bottom was subsequently analyzed by AFM with a Bruker Dimension Icon AFM ScanAsyst in air with an AFM tip made out of silicon nitride. Its morphology, surface orientation, and composition were analyzed with a Zeiss Merlin electron microscope equipped with a Gemini 2 electron gun, an EBSD NordlysNano system from Oxford Instruments, and an X-Max EDX system from Oxford Instruments. The crater depth profiles and the crater topography were measured with a Veeco Dektak profilometer and a Keyence VK-X1000 confocal laser scanning microscope.

The target materials STO, LAO, and YAG have bandgaps of 3.2, 5.6 and 6.5 eV, respectively. In the case of STO, photon excitation by 248 nm KrF excimer radiation is sufficient to generate electron-hole pairs directly by photon-induced interband transitions. In contrast, nonlinear effects for the other two target materials and multiphoton absorption must

occur for photon absorption. Their thermal conductivities and melting temperatures are close to each other (see Table 1), while the coefficient of thermal expansion of STO is about an order of magnitude larger than that of LAO and YAG. In the case of the STO target, three different crystal orientations (001), (011), and (111) were studied in particular. The LAO surface orientation was (102), and that of YAG was (001).

### 3 Results and discussion

#### 3.1 Image quality at the target surface

Profilometer scans were used to verify the quality of the rectangular ablation craters along their short and long sides for the six laser fluences on the polycarbonate film used in this work. The crater rim was additionally analyzed by confocal laser scanning microscopy. Figure 2a shows depth profiles for laser pulse fluences between 1 and 6 J cm<sup>-2</sup> after applying 30 laser pulses. The depth profiles present a well-defined crater with increased crater depth and laser fluence. The crater bottom remains well defined up to a laser fluence of 4 J cm<sup>-2</sup>, at higher fluences, an uneven crater bottom is

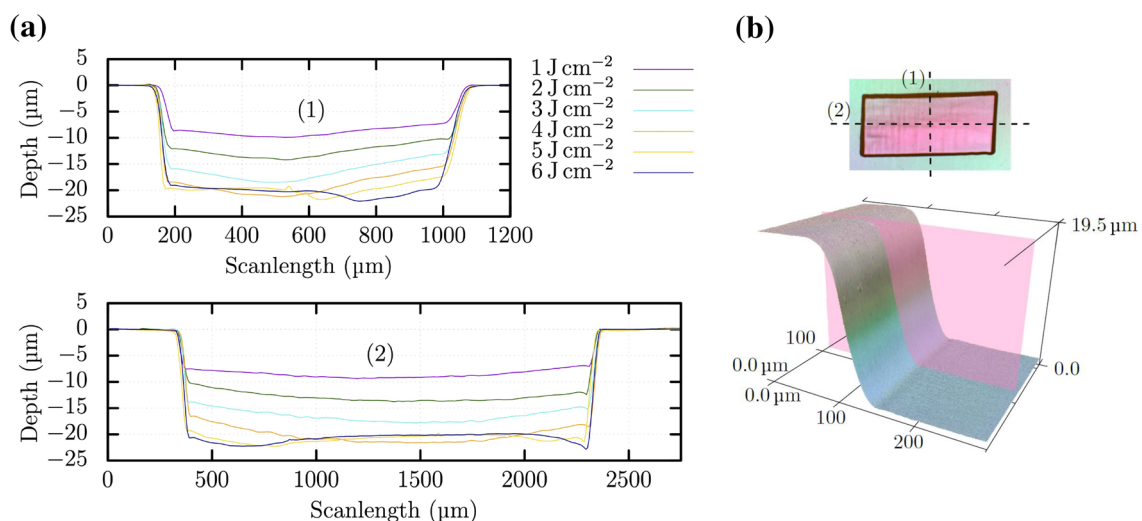


**Fig. 2** **a** Depth profiles in two directions of the laser craters on polycarbonate from different laser fluences. **b**-top Differential interference contrast image of the crater irradiated with 4 J cm<sup>-2</sup>, marked are the scan lines from a). **b**-bottom Crater rim from the crater irradiated with 6 J cm<sup>-2</sup>

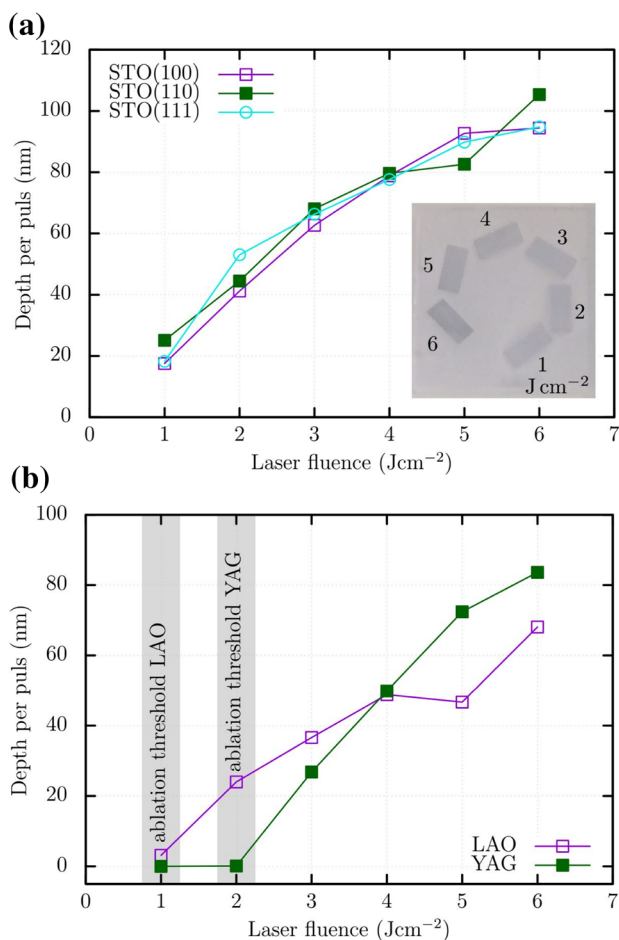


**Fig. 3** **a** Ablated target thickness per laser pulse for the single crystal targets of STO with the orientations (001), (011) and (111). The inset shows an optical photograph of a 10 × 10 mm<sup>2</sup> STO target with the 6 laser ablated surface positions. **b** Ablated target thickness for (102) LAO and (001) YAG versus fluence per laser pulse

visible, which can be caused by carbonization of the polycarbonate, which occurs due to the high thermal energy [22]. The long crater side agrees with the intended aperture image ratio 5 to 1. The short side shows a ratio 6.5 to 1, which is due to the inclination angle of the laser beam onto the target surface. This inclination leads to a tilt of the focus plane and, therefore, to a small gradient in the laser fluence. The two scan directions are shown in a differential interference contrast image in Fig. 2b-top. The laser scanning microscopy image in Fig. 2b-bottom of the crater rim irradiated with 6 J cm<sup>-2</sup> presents a very steep drop with a width of only ≈ 50 μm.

### 3.2 Ablated target thickness per laser pulse

The ablated thickness per laser pulse for all target materials investigated in this work is shown in Fig. 3. The

thickness was measured by profilometer scans analogously to Fig. 2a. In Fig. 3a, the ablated thickness per laser pulse is the same for all three crystal orientations of STO and laser fluences, whereby the ablation threshold lies below 1 J cm<sup>-2</sup>. With increasing laser pulse fluence, the ablated layer thickness per laser pulse increases sub-linearly, which can be attributed to absorption and mirror effects due to the laser-generated plasma and free charge carriers [23].

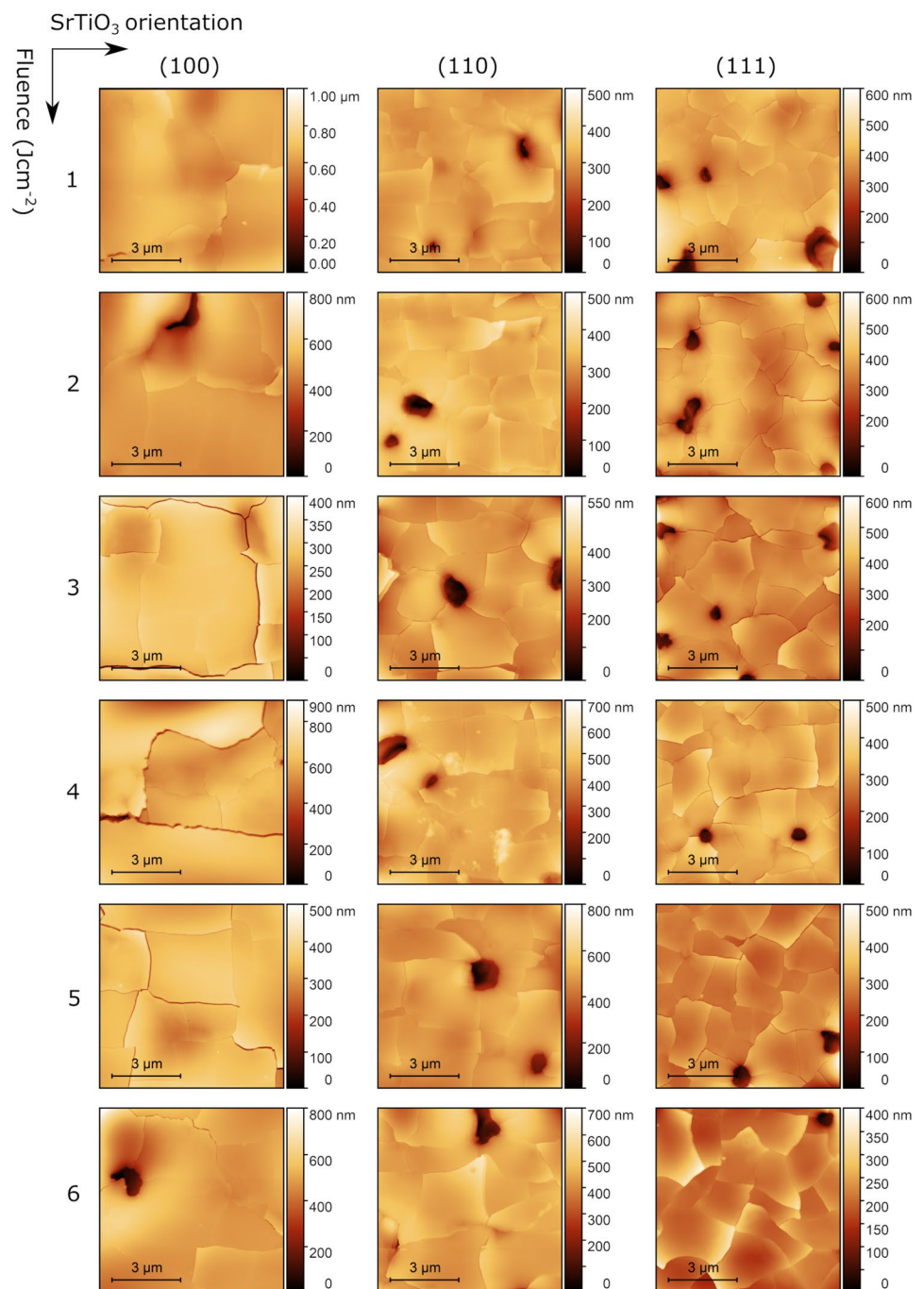
For the LAO and YAG target depicted in Fig. 3b, an ablation threshold of more than 1 J cm<sup>-2</sup> and 2 J cm<sup>-2</sup> respectively, can be determined, which is mainly a consequence of the need of nonlinear photon absorption mechanisms due to their wide bandgaps. Above the ablation threshold, the ablated thickness per pulse increases sublinearly with the laser pulse fluence for LAO, whereas in the case of YAG, a nearly linear increase is found.

### 3.3 Topography and morphology of the laser-ablated STO targets

AFM images of the crater bottoms for the STO targets with surface orientation (001), (011) and (111) versus the laser pulse fluence are shown in Fig. 4. Cracks can be identified with partially upward curved layer separations in case of all crystal orientations and fluences. The crack density shows a dependency on the crystal orientation and increases from the surface orientation (001) to (011) and further to (111) as shown in the crystal surface orientation—laser fluence matrix depicted in Fig. 4. In addition, the formation of holes with a diameter ranging from ≈ 0.5 to 1 μm can be detected, which appear to form preferentially along a fracture line. The SEM image taken from a cleaved STO target at the ablation crater irradiated with 6 J cm<sup>-2</sup> is shown in Fig. 5a. The thickness of the partially delaminated layer is ≈ 350 nm and independent of the laser fluence (corresponding series of SEM images not shown). Furthermore, circular and ellipsoidal voids can be identified below the partially delaminated layer.

It is known that STO has a dynamic oxygen exchange chemistry, starting already at relatively low temperatures [24–26]. The voids below the partially delaminated layer (see Fig. 5a) and holes observed on the surface (see Fig. 4) can be formed by decomposition liberating volatile oxygen during the short heating period of the ablation process. To measure the oxygen content of the irradiated area, spatially resolved energy-dispersive X-ray spectroscopy was performed. Figure 6 shows in (a) the crater rim on the (001) oriented STO target surface irradiated with a laser fluence of 6 J cm<sup>-2</sup> and the corresponding EDX scan in (b). The EDX signal reveals an apparent reduction of the oxygen content of 3.1% within the crater. Due to the increase in noise of the signal within the crater caused by the rough surface, a

**Fig. 4** AFM images of the crater bottom for the STO crystal targets with surface orientation (001), (011), and (111) versus laser pulse fluence. Visible are cracks in the surface with partially upward curved layer separations in case of all crystal orientations and fluences. However, the crack density increases with laser pulse fluence and with orientation from (001), (011) to (111). Another surface feature is the formation of holes with a diameter of  $\approx 0.5 \mu\text{m}$



change in the Sr/Ti ratio could not be determined. The (110) and (111) STO orientations showed similar results.

From these observations, we conclude that this layer is formed by melting and release of oxygen gas, followed by rapid recrystallization. The formed voids and recrystallization process leads to mechanical strain, cracks, and delamination, which is most likely the consequence of the large expansion coefficient of STO (see Table 1). The dependence of crack density on crystal orientation shows preferential cracking along the main lattice planes. This is in good

agreement with nanoindentation tests performed on STO [27], where the crack formation happened preferably along the (110) plane when the (001) surface was indented. Cracking during laser irradiation of STO has already been reported [28, 29] and explained by a thermal shock effect due to the low thermal conductivity of  $12 \text{ W K}^{-1}\text{m}$  of STO, and that fs-pulse ablation can suppress it [29]. However, details on the underlying process were neither discussed nor investigated.

To elucidate the crystallinity of the irradiated target surface, electron backscatter diffraction (EBSD) images of the

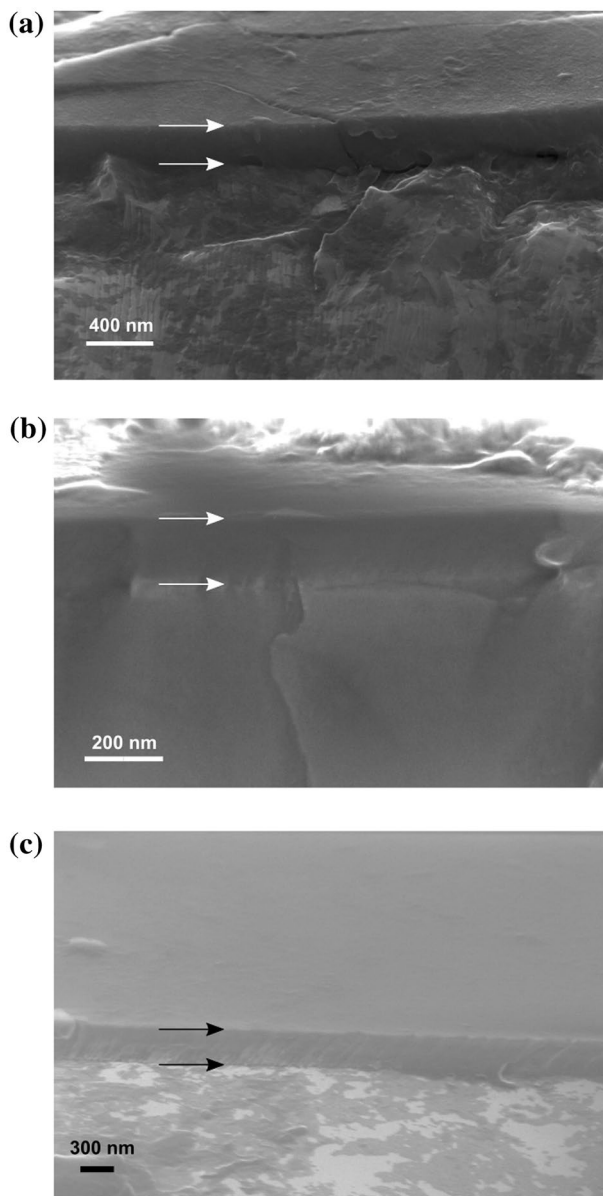


**Fig. 5** **a**, **b** and **c** SEM side view images of the cleaved targets STO, LAO, and YAG (SEM sample holder tilt angle  $30^\circ$ ). For each substrate studied, an identifiable layer forms in the ablated area (horizontal arrows indicate the top and bottom of this layer)

crater bottom of STO (001), (011) and (111) were taken. Figure 7a, c and e show SEM images of the laser ablated (001), (011), and (111) STO target surface together with corresponding overlay images of the Kernel Average Misorientation (KAM) and the corresponding band contrast (BC) image, shown in Fig. 7b, d and f, respectively. The KAM images were generated by numerical analysis of the Kikuchi patterns originating from multiple elastic electron scattering. The laser pulse fluence was  $4 \text{ J cm}^{-2}$  for all surface

orientations of STO. This series of images shows that the STO material in the ablated area is single crystalline to the surface and has recovered its original crystalline orientation. The observed crystalline misorientation is mainly due to bending at the layer boundaries.

### 3.4 Topography and morphology of the laser-ablated LAO and YAG target

Figures 8 and 9 show optical microscopy and laser microscopy images of the craters from LAO and YAG, respectively. In the case of YAG, no significant dependency of the topography with the laser fluence could be observed. Therefore, Fig. 8 only shows the crater with the highest fluence of  $6 \text{ J cm}^{-2}$ , which presents a flat surface with tiny bubbles on the left side of the image and large chipped areas with conchoidal fractures on the right side. In contrast to the YAG crater, the crater bottoms of the LAO target show significant changes with increasing laser fluence. Figure 9 presents very smooth surfaces and an increase in the number of thin hairline cracks on the LAO surface with increasing laser fluence. The laser microscopy images also show round structures, which have an inverse dependency of their number with increasing laser fluence. These structures can be attributed to irregular cracks located underneath the surface, which have already been observed in LAO [30] after irradiation with a KrF excimer laser. The observed dependency of their number with the laser fluence could be caused by a variation of the distance of these cracks from the surface with increasing laser fluence. Since the focus of the laser microscope is on the target surface, an increased distance of these subsurface cracks brings them out of focus, which can be observed in Fig. 9.

AFM images for the ablated areas on LAO and YAG are shown in Fig. 10. The AFM images of YAG were taken on the flat, non-chipped surfaces (see. Fig. 8). For all laser fluences, the irradiated target surface of LAO remains very flat, except for fluence  $4 \text{ J cm}^{-2}$ , where some particles were found on the ablated surface. Similarly, a very flat ablated surface in the case of YAG at the laser fluences of 3 and  $4 \text{ J cm}^{-2}$  was found. At fluences of 5 and  $6 \text{ J cm}^{-2}$  elongated structures reminiscent of splashes of molten material are detectable. Figure 5b, c shows SEM images taken from a cleaved LAO and YAG target at the ablation craters, irradiated with  $6 \text{ J cm}^{-2}$ . Both target materials show a distinct layer which has a thickness of  $\approx 290 \text{ nm}$  for LAO and  $\approx 350 \text{ nm}$  for YAG, respectively. In contrast to the layer in STO in Fig. 5a, both layers show no signs of voids, cracks, or delamination features. Analogously to the observed STO layer, the layers observed on LAO and YAG also do not

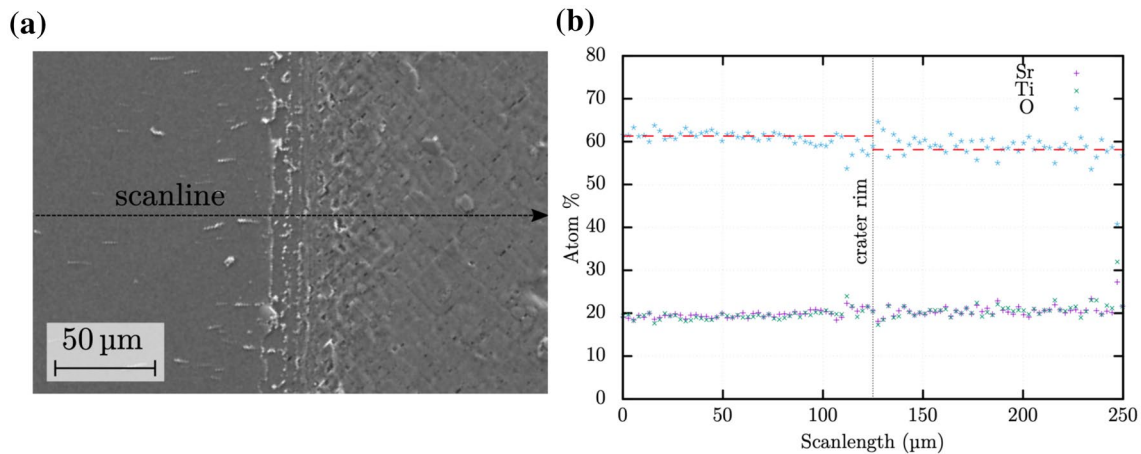


**Fig. 6** SEM image of the crater rim irradiated with a laser fluence of  $6 \text{ J cm}^{-2}$  on a (001) STO target in **a** and the corresponding EDX scan profile for the elements Sr, Ti and O in **b**. The EDX scan shows a reduction in the oxygen content in the irradiated area

show a significant dependency of their thickness with laser fluence.

Similar to the STO targets, spatially resolved energy-dispersive X-ray spectroscopy was performed to measure possible variations of the oxygen content of the irradiated areas. For these measurements, both samples were coated with a 15 nm thick carbon layer to avoid the charging effect of the two electrically isolating substrates. Figure 11 shows in **a** a SEM image of the crater rim on the YAG target surface irradiated with a laser fluence of  $6 \text{ J cm}^{-2}$  and the corresponding EDX scan in **(b)**. The EDX signal reveals no change in the target stoichiometry between the crater and the non-irradiated surface. The EDX measurement of the LAO crater rim, irradiated with  $6 \text{ J cm}^{-2}$  is shown in Fig. 12. The EDX measurement shows a slight change of around 1% for both the oxygen and aluminum content between the crater and the non-irradiated target surface. Due to the increase in noise on the crater signal, there is likely no change in the stoichiometry between the irradiated and non-irradiated area. The very flat surface observed in the AFM images combined with the thin hairline cracks, which—in contrast to the surface features observed on STO—do not bend upwards at the edges, gives rise to the conclusion that no significant outgassing takes place and the stoichiometry is unaffected by the laser irradiation.

EBSD scans for the LAO and YAG samples were not possible due to the carbon coating. The low electrical conductivity of these materials also agrees well with the fact that their oxygen stoichiometry remains unchanged during

the ablation process. In contrast, STO loses oxygen, resulting in an electrically conductive surface, thus eliminating the need to coat the surface with carbon and therefore EBSD measurements could be performed.

The lack of quantitative dynamic thermophysical parameters of STO, LAO, and YAG during all stages of the ablation process makes it difficult to determine the decisive material properties explaining the observed differences. Assisted by the oxygen release and oxygen diffusion in STO in reducing atmosphere, the shock-wave energy leads to the delamination of a thin layer. The formation of voids and holes, also originating from the oxygen release, further encourages the formation of cracks and, therefore, delamination, driven by the large expansion coefficient of STO (see Table 1). In the case of the target materials LAO and YAG, the energy is mainly released by conchoidal fractures in the case of YAG and thin hairline cracks and irregular under-surface cracks in the case of LAO. These findings are probably due to their more significant hardness [31] and higher temperature stability concerning oxygen release and oxygen diffusion in a reducing atmosphere compared to STO [26, 32]. The observed difference between YAG and LAO could also be the consequence of the lower melting point of YAG in comparison to LAO (see Table 1), leading to a rapid melting of the top layer followed by recrystallization. This hypothesis can be supported by the observation of bubbles within this molten layer in the microscopy image in Fig. 8 and the increase in splashes of molten material in the AFM images in Fig. 10.

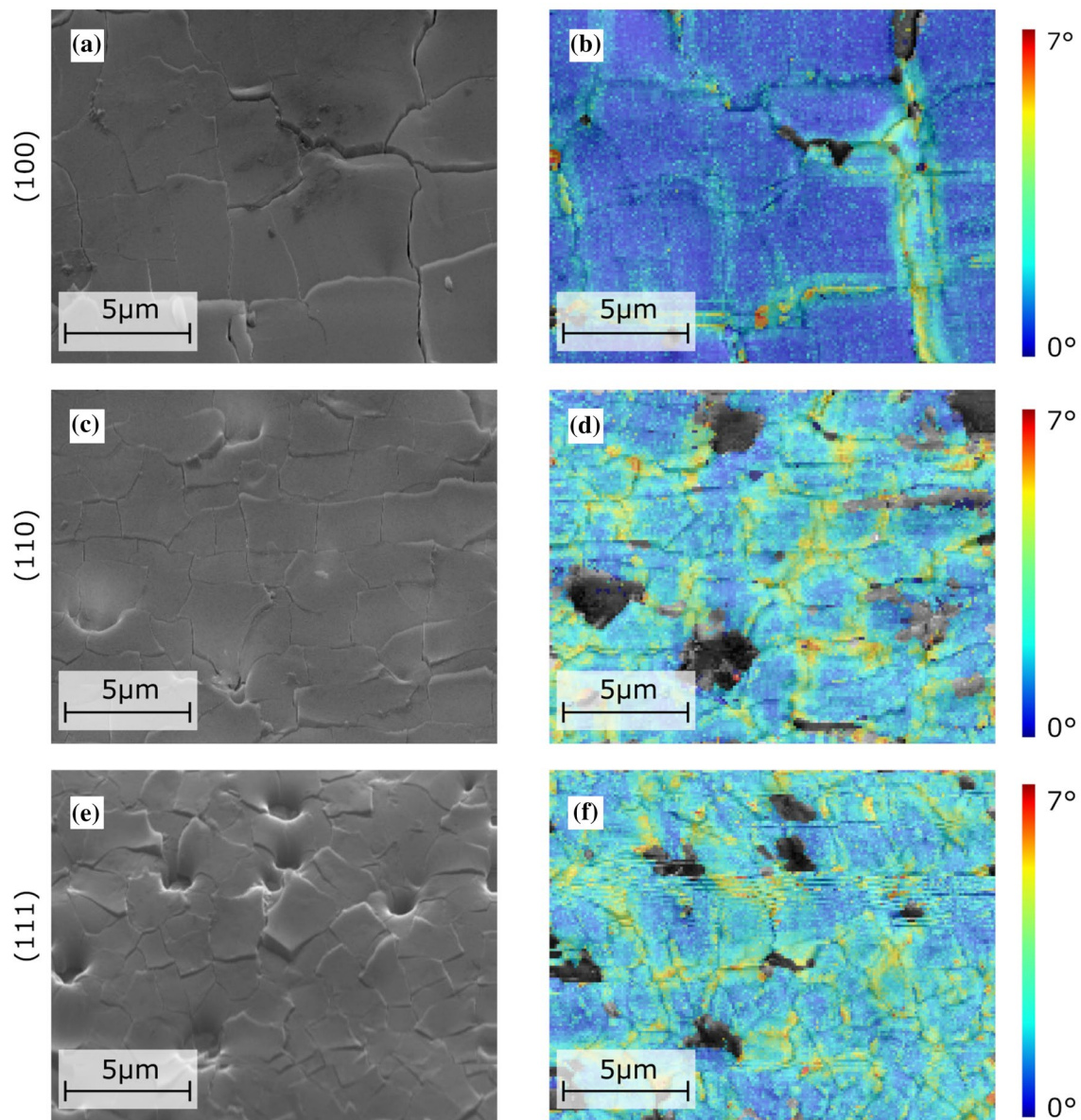


**Fig. 7** **a**, **c** and **e** SEM images of the ablated areas of (001), (011) and (111) oriented STO laser ablated with  $4 \text{ J cm}^{-2}$ . **b**, **d** and **f** The corresponding overlays of the KAM and BC images. The color code indicates the laterally resolved crystal misorientation in degree

## 4 Conclusion

We investigated the changes of the surfaces of single crystalline PLD target materials STO, LAO, and YAG after ablation with a series of KrF excimer laser pulses in terms of topography, crystallinity, and stoichiometry in the laser fluence range from 1 to  $6 \text{ J cm}^{-2}$ . The formation of a several hundred nm thick layer could be observed for all target materials studied. Hole formation, cracking and partial delamination of this layer was observed at STO for all laser fluences, whereby the crack density and hole formation increase with surface orientation from (001) through (011)

to (111). Compared to STO, the surfaces of the LAO target shows only thin hairline cracks above  $2 \text{ J cm}^{-2}$  and no delamination or hole formation. The YAG target remained free of cracks and delamination of the layer but exhibited conchoidal fractures and large chipped areas, independent from the laser fluence. We conclude that thermal shock is not the only mechanism that must be considered to explain the observed surface features, but also mechanical strain due to thermal expansion and decomposition due to the release of oxygen in the case of STO. For STO, EBSD images also show that the delaminated layer is single crystalline. The layers formed are thicker than the layer ablated



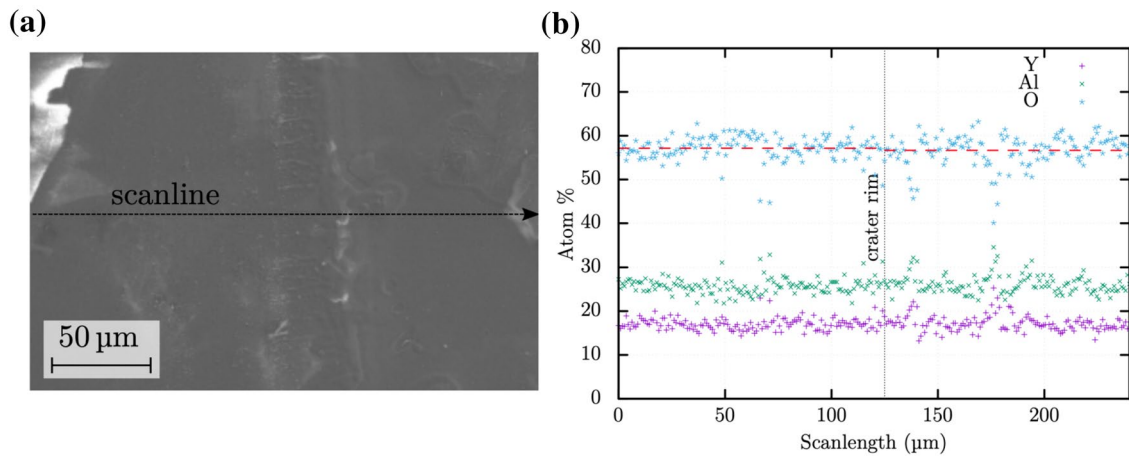


**Fig. 11** SEM image of the crater rim irradiated with a laser fluence of  $6 \text{ J cm}^{-2}$  on a YAG target in **a** and the corresponding EDX scan profile for the elements Y, Al and O in **b**

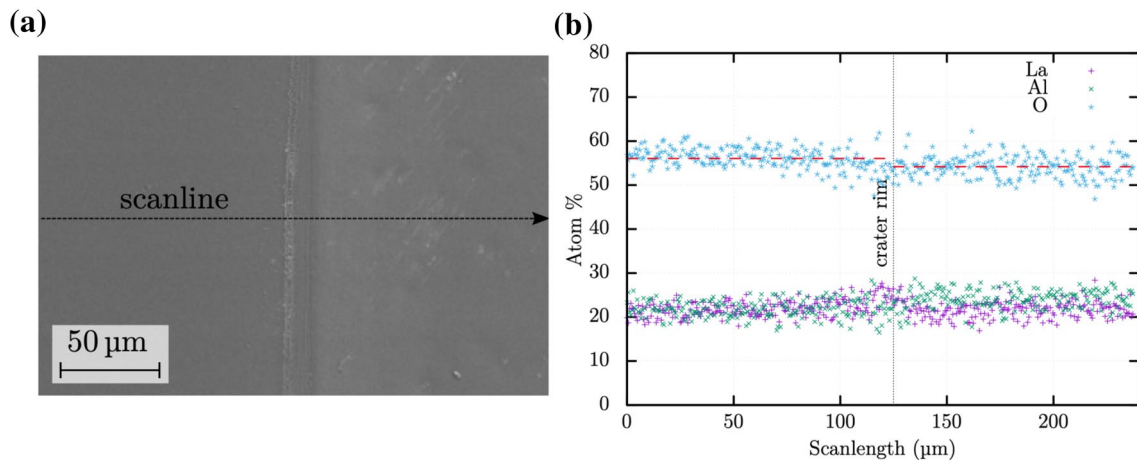


**Fig. 12** SEM image of the crater rim irradiated with a laser fluence of  $6 \text{ J cm}^{-2}$  on a LAO target in **a** and the corresponding EDX scan profile for the elements La, Al and O in **b**

by a single laser pulse for all three target materials. We conclude that this layer is formed by periodic melting and recrystallization with each laser pulse as the material is ablated from its surface. These results might help to optimize target selection for PLD or patterning by excimer laser irradiation of these materials.

**Funding** Open Access funding enabled and organized by Projekt DEAL.

**Open Access** This article is licensed under a Creative Commons Attribution 4.0 International License, which permits use, sharing, adaptation, distribution and reproduction in any medium or format, as long as you give appropriate credit to the original author(s) and the source,

provide a link to the Creative Commons licence, and indicate if changes were made. The images or other third party material in this article are included in the article's Creative Commons licence, unless indicated otherwise in a credit line to the material. If material is not included in the article's Creative Commons licence and your intended use is not permitted by statutory regulation or exceeds the permitted use, you will need to obtain permission directly from the copyright holder. To view a copy of this licence, visit <http://creativecommons.org/licenses/by/4.0/>.

**Open Access** This article is licensed under a Creative Commons Attribution 4.0 International License, which permits use, sharing, adaptation, distribution and reproduction in any medium or format, as long as you give appropriate credit to the original author(s) and the source, provide a link to the Creative Commons licence, and indicate if changes were made. The images or other third party material in this article are included in the article's Creative Commons licence, unless indicated otherwise in a credit line to the material. If material is not included in

the article's Creative Commons licence and your intended use is not permitted by statutory regulation or exceeds the permitted use, you will need to obtain permission directly from the copyright holder. To view a copy of this licence, visit <http://creativecommons.org/licenses/by/4.0/>.

## References

- N. Varkentina, N. Sanner, M. Lebugle, M. Sentis, O. Utéza, Absorption of a single 500 fs laser pulse at the surface of fused silica: energy balance and ablation efficiency. *J. Appl. Phys.* **114**(17), 173105 (2013). <https://doi.org/10.1063/1.4829015>
- B.C. Stuart, M.D. Feit, S. Herman, A.M. Rubenchik, B.W. Shore, M.D. Perry, Nanosecond-to-femtosecond laser-induced breakdown in dielectrics. *Phys. Rev. B* **53**(4), 1749–1761 (1996). <https://doi.org/10.1103/PhysRevB.53.1749>
- M.D. Perry, B.C. Stuart, P.S. Banks, M.D. Feit, V. Yanovsky, A.M. Rubenchik, Ultrashort-pulse laser machining of dielectric materials. *J. Appl. Phys.* **85**(9), 6803–6810 (1999). <https://doi.org/10.1063/1.370197>
- M. Stafe, A. Marcu, N. Puscas, Pulsed Laser Ablation of Solids, 1st edn. Springer Series in Surface Sciences, vol. 53, p. 233. Springer, Berlin, Heidelberg (2014). <https://doi.org/10.1007/978-3-642-40978-3>
- V. Cerletti, W.A. Coish, O. Gywat, D. Loss, Recipes for spin-based quantum computing. *Nanotechnology* **16**(4), 27–49 (2005). <https://doi.org/10.1088/0957-4484/16/4/r01>
- D. Loss, D.P. DiVincenzo, Quantum computation with quantum dots. *Phys. Rev. A* **57**(1), 120–126 (1998). <https://doi.org/10.1103/PhysRevA.57.120>
- P. Liang, R.R. Hu, C. Chen, V.V. Belykh, T.Q. Jia, Z.R. Sun, D.H. Feng, D.R. Yakovlev, M. Bayer, Room-temperature electron spin dynamics of Ce<sup>3+</sup> ions in a YAG crystal. *Appl. Phys. Lett.* **110**(22), 222405 (2017). <https://doi.org/10.1063/1.4984232>
- C. Brooks, R. Wilson, A. Schäfer, J. Mundy, M. Holtz, D. Muller, J. Schubert, D. Cahill, D. Schlom, Tuning thermal conductivity in homoepitaxial SrTiO<sub>3</sub> films via defects. *Appl. Phys. Lett.* **107**, 051902 (2015). <https://doi.org/10.1063/1.4927200>
- Y. Lu, D. Jia, F. Gao, T. Hu, Z. Chen, First-principle calculations of the thermal properties of SrTiO<sub>3</sub> and SrO(SrTiO<sub>3</sub>)<sub>n</sub> (n=1,2). *Solid State Commun.* **201**, 25–30 (2015). <https://doi.org/10.1016/j.ssc.2014.09.011>
- D. De Ligny, P. Richet, High-temperature heat capacity and thermal expansion of SrTiO<sub>3</sub> and SrZrO<sub>3</sub> perovskites. *Physical review. B, Condensed matter* **53**, 3013–3022 (1996). <https://doi.org/10.1103/PhysRevB.53.3013>
- Muhamad, Norhizatol Fashren, Maulat Osman, Rozana Aina, Idris, Mohd Sobri, Mohd Yasin, Mohd Najib: Physical and electrical properties of SrTiO<sub>3</sub> and SrZrO<sub>3</sub>. *Epj Web of Conferences* **162**, 01052 (2017). <https://doi.org/10.1051/epjconf/201716201052>
- M. Crespillo, J. Graham, F. Agulló-López, Z. Yanwen, W. Weber, Recent advances on carrier and exciton self-trapping in strontium titanate: understanding the luminescence emissions. *Crystals* **9**, 95 (2019). <https://doi.org/10.3390/cryst9020095>
- Peter C. Michael, B.Y. John U., Trefny: Thermal transport properties of single crystal lanthanum aluminate. *J. Appl. Phys.* **72**, 107–109 (1992). <https://doi.org/10.1063/1.352166>
- N. Vourdas, E. Marathoniti, P.K. Pandis, C. Argiris, G. Sourkouni, C. Legros, S. Mirza, V.N. Stathopoulos, Evaluation of LaAlO<sub>3</sub> as top coat material for thermal barrier coatings. *Trans. Nonferrous Metals Soci. China* **28**(8), 1582–1592 (2018). [https://doi.org/10.1016/S1003-6326\(18\)64800-9](https://doi.org/10.1016/S1003-6326(18)64800-9)
- S.V. Ushakov, A. Navrotsky, Direct measurement of fusion enthalpy of LaAlO<sub>3</sub> and comparison of energetics of melt, glass, and amorphous thin films. *J. Am. Ceramic Soc.* **97**(5), 1589–1594 (2014). <https://doi.org/10.1111/jace.12785>
- K. Potzger, S. Zhou, ChemInform abstract: Non-dms related ferromagnetism in transition metal doped zinc oxide. *ChemInform* **41** (2010). <https://doi.org/10.1002/pssb.200844272>
- T. Fan, D. Ripin, R. Aggarwal, J. Ochoa, B. Chann, M. Tilleman, J. Spitzberg, Cryogenic Yb<sup>3+</sup>-Doped solid-state lasers. *Selected Topics in Quantum Electronics, IEEE Journal of* **13**, 448–459 (2007). <https://doi.org/10.1109/JSTQE.2007.896602>
- D. Brown, J. Singley, K. Kowalewski, J. Guelzow, V. Vitali, High sustained average power cw and ultrafast Yb:YAG near-diffraction-limited cryogenic solid-state laser. *Optics express* **18**, 24770–92 (2010). <https://doi.org/10.1364/OE.18.024770>
- R. Aggarwal, D. Ripin, J. Ochoa, T. Fan, Measurement of thermo-optic properties of Y<sub>3</sub>Al<sub>5</sub>O<sub>12</sub>, Lu<sub>3</sub>Al<sub>5</sub>O<sub>12</sub>, YAlO<sub>3</sub>, LiYF<sub>4</sub>, LiLuF<sub>4</sub>, BaY<sub>2</sub>F<sub>8</sub>, KGd(WO<sub>4</sub>)<sub>2</sub>, and KY(WO<sub>4</sub>)<sub>2</sub> laser crystals in the 80–300 K temperature range. *J. Appl. Phys.* **98**, 103514–103514 (2005). <https://doi.org/10.1063/1.2128696>
- B. Bhattacharyya, B. Doloi, Machining processes utilizing thermal energy, Chap. 4. In: Bhattacharyya, B., Doloi, B. (eds.) *Modern Machining Technology*, pp. 161–363. Academic Press (2020). <https://doi.org/10.1016/B978-0-12-812894-7.00004-9>
- V.P. Krokhin, V.S. Bessmernyi, O.V. Puchka, O.N. Shvyrkina, Synthesis of A-Al garnet. *Glass Ceramics* **55**(5), 151–152 (1998). <https://doi.org/10.1007/BF02694729>
- G. Chen, Z.K. Wang, K.K. Tan, H. Xie, X. Wang, Investigation on fiber laser irradiation of transparent polycarbonate. *J. Laser Appl.* **32**(3), 032009 (2020). <https://doi.org/10.2351/7.0000172>
- I.B. Földes, D. Csáti, F.L. Szűcs, Sándor Szatmári: Plasma mirror and temperature evolution for short pulse KrF lasers. *Radiation Effects Defects Solids* **165**(6–10), 429–433 (2010). <https://doi.org/10.1080/10420151003715457>
- M. Mori, Z. Wang, T. Itoh, Pore Formation during Sintering of (Sr<sub>0.9</sub>La<sub>0.1</sub>)<sub>1-x</sub>TiO<sub>3+δ</sub> Perovskites (X=0, 0.04) Synthesized by the Pechini Method. *Electrochemistry* **79**(9), 688–695 (2011). <https://doi.org/10.5796/electrochemistry.79.688>
- M. Stöber, C. Cherkouk, T. Leisegang, M. Schelter, J. Zosel, J. Walter, J. Hanzig, M. Zschornak, S. Prucnal, R. Böttger, D.C. Meyer, Oxygen exchange kinetics of SrTiO<sub>3</sub> single crystals: A non-destructive. *Quantitative Method* **53**(6), 1800004 (2018). <https://doi.org/10.1002/crat.201800004>
- N. Vourdas, E. Marathoniti, P.K. Pandis, C. Argiris, G. SOURKOUNI, C. Legros, S. Mirza, V.N. Stathopoulos, Evaluation of LaAlO<sub>3</sub> as top coat material for thermal barrier coatings. *Trans. Nonferrous Metals Soc. China* **28**(8), 1582–1592 (2018). [https://doi.org/10.1016/S1003-6326\(18\)64800-9](https://doi.org/10.1016/S1003-6326(18)64800-9)
- X. Fang, K. Ding, C. Minnert, A. Nakamura, K. Durst, Dislocation-based crack initiation and propagation in single-crystal SrTiO<sub>3</sub>. *J. Materials Sci.* **56**(9), 5479–5492 (2021). <https://doi.org/10.1007/s10853-020-05587-2>
- F. Benítez, F. Sánchez, V. Trtík, M. Varela, M. Bibes, B. Martínez, J. Fontcuberta, Laser irradiation of SrTiO<sub>3</sub> single crystals. *Appl. Phys. A* **69**(1), 501–504 (1999). <https://doi.org/10.1007/s003390051452>
- S. Zoppel, D. Gray, M. Farsari, R. Merz, G.A. Reider, C. Fotakis, Elimination of cracking during UV laser ablation of SrTiO<sub>3</sub> single crystals by employing a femtosecond laser. *Appl. Surface Sci.* **252**(5), 1910–1914 (2005). <https://doi.org/10.1016/j.apsusc.2005.07.072>
- R. Aguiar, F. Sánchez, C. Ferrater, M. Varela, Effects of excimer-laser irradiation of LaAlO<sub>3</sub> (100) single crystals: Influence on superconducting YBa<sub>2</sub>Cu<sub>3</sub>O<sub>7-x</sub> film growth **65**(4), 429–436 (1997). <https://doi.org/10.1007/s003390050604>

31. R.A. Schultz, M.C. Jensen, R.C. Bradt, Single crystal cleavage of brittle materials. *Int. J. Fract.* **65**, 291–312 (1994). <https://doi.org/10.1007/BF00012370>
32. I. Georgiopoulos, N. Vourdas, S. Mirza, C. Andreouli, V. Stathopoulos, LaAlO<sub>3</sub> as overlayer in conventional thermal barrier coatings. *Proc. Struct. Integrity* **10**, 280–287 (2018). <https://doi.org/10.1016/j.prostr.2018.09.039>

**Publisher's Note** Springer Nature remains neutral with regard to jurisdictional claims in published maps and institutional affiliations.